

RESEARCH

Open Access



# Single BMSC-derived cartilage organoids for gradient heterogeneous osteochondral regeneration by leveraging native vascular microenvironment

Zhenying Chen<sup>2†</sup>, Qitao Bo<sup>3†</sup>, Chao Wang<sup>3†</sup>, Yong Xu<sup>3,4\*</sup>, Xiang Fei<sup>3\*</sup> and Ru Chen<sup>1\*</sup>

## Abstract

Heterogeneous osteochondral regeneration remains a significant challenge due to the distinct microenvironments across the cartilage, calcified cartilage, and subchondral bone layers. The natural gradient of vascularization from the superficial to deep layers of osteochondral tissue plays a critical role in guiding the differentiation of bone marrow stem cells (BMSCs) into chondrocytes and osteoblasts. In this study, we propose a strategy for gradient heterogeneous osteochondral regeneration using cartilage organoids derived from single BMSCs, leveraging the natural vascularization gradient within osteochondral tissue. We successfully isolated BMSCs from rabbits and generated cartilage organoids via in vitro three-dimensional chondrogenic culture. To mimic the pro-vascular microenvironment, we introduced vascular endothelial growth factor, which promoted the hypertrophic differentiation of the cartilage organoids. We then prepared cartilage organoid/GelMA complexes, with or without the anti-vascular drug Axitinib, and implanted them subcutaneously in nude mice. The vascularized subcutaneous microenvironment induced osteogenic differentiation, while Axitinib treatment created an anti-vascular microenvironment, inhibiting osteogenesis and preserving chondrogenesis within the complexes. Both in vitro and in vivo data demonstrated the crucial role of the vascular microenvironment in regulating osteogenic differentiation of cartilage organoids. Finally, organoid/GelMA cylinders were implanted into a rabbit osteochondral defect, where the gradient vascularization at the defect site guided the organoids to differentiate into both cartilage and bone. This single BMSC-derived cartilage organoid approach enables precise gradient heterogeneous osteochondral regeneration, guided by the natural microenvironment within the osteochondral defect site, representing a significant advancement for clinical applications.

**Keywords** Cartilage organoid, BMSC, Gradient vascular microenvironment, Osteochondral regeneration, Tissue engineering

<sup>†</sup>Zhenying Chen, Qitao Bo and Chao Wang these authors are equal to this work.

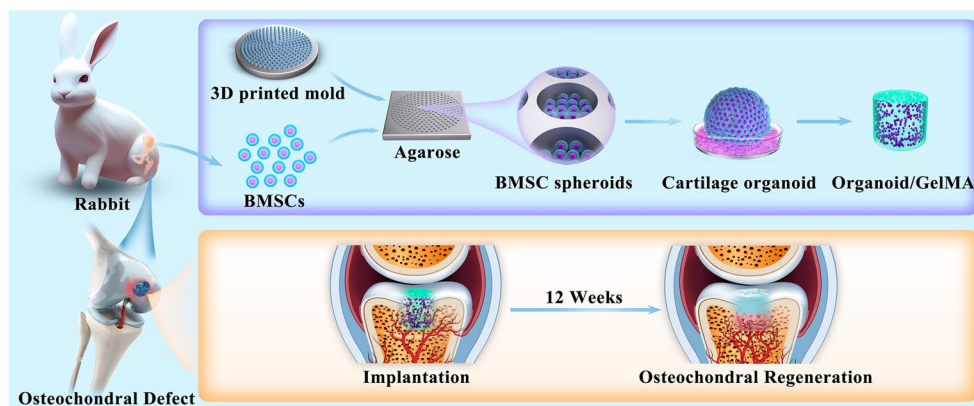
\*Correspondence:

Yong Xu  
xuyong@tongji.edu.cn  
Xiang Fei  
387681863@qq.com  
Ru Chen  
cr106@163.com

Full list of author information is available at the end of the article



## Graphical Abstract



## Introduction

Injuries to articular cartilage and subchondral bone, typically caused by trauma or osteoarthritis, often progress to osteochondral defects (OCDs) [1]. The natural osteochondral structure of the knee joint consists of three layers: articular cartilage, calcified cartilage, and subchondral bone, which transition seamlessly with gradient heterogeneity [2]. Articular cartilage, primarily composed of collagen type II and proteoglycans, is avascular and relies on synovial fluid for oxygen and nutrients. In contrast, subchondral bone is a highly vascularized hard tissue, with its extracellular matrix (ECM) comprising collagen type I and hydroxyapatite, providing structural support and stiffness. The calcified cartilage layer serves as a transitional structure, naturally bridging the articular cartilage and subchondral bone. Together, these three components form a gradient heterogeneous osteochondral tissue. However, the regeneration and repair of OCDs face significant challenges: the avascular nature of cartilage limits its intrinsic self-repair capabilities [3], and the gradient heterogeneity complicates biomimetic repair strategies [4]. These factors make the development of effective therapeutic strategies for OCD a critical challenge in current research.

Despite the availability of various clinical treatments for OCDs, such as arthroscopic debridement, microfracture, stem cell transplantation, and autologous/allogeneic grafts, none have achieved integrated regeneration of cartilage and subchondral bone with gradient heterogeneity [5, 6]. These methods often fail to reconstruct the natural gradient structure, and graft failure remains a significant issue. Traditional tissue engineering approaches, while showing some progress in animal models [7, 8], still struggle to replicate the smooth transitions found

in native osteochondral tissues, leaving a gap between research outcomes and clinical needs [9].

Organoid technology, which enables the construction of functional tissues *in vitro*, offers a promising avenue for OCD repair. Organoids are 3D cell spheres derived from pluripotent or adult stem cells through self-assembly, and they have been widely used in organ development, disease modeling, drug discovery, and regenerative medicine [10]. The concept of organoids dates back to the early twentieth century [11], but significant progress was made in 2009 when Clevers and colleagues successfully constructed self-organized 3D structures replicating the intestinal epithelium [12]. Since then, organoid research has expanded to various tissues, including the pancreas, liver, and lungs [13]. However, the application of organoids in OCD repair is still in its early stages, with numerous technical challenges to overcome.

Cartilage organoid construction is relatively mature, with successful examples dating back to the 1990s [14]. For instance, spherical cartilage organoids have been developed, capable of secreting endogenous ECM to protect chondrocytes during regeneration [15, 16]. In contrast, bone organoid construction remains challenging due to the need for precise regulation of ECM mineralization and deposition [17]. Although some progress has been made, such as the use of BMP-2-loaded scaffolds to induce bone formation *in vivo* [18], no mature methods for bone organoid construction have been established. Therefore, a key challenge in preparing gradient heterogeneous osteochondral tissues using organoid technology lies in how to guide the regeneration of subchondral bone tissue beneath the cartilage layer.

A key challenge in OCD repair lies in integrating cartilage and bone organoids to mimic the natural gradient

structure. Constructing separate cartilage and bone organoids may be feasible, but this approach faces significant scientific and practical challenges, including the lack of established protocols for bone organoids, the complexity of simultaneously constructing two distinct organoids, and the difficulty of achieving a seamless gradient transition between them. Therefore, constructing organoids from the same type of stem cells that can simultaneously guide the regeneration of both cartilage and bone tissues may offer a solution to these problems. By using appropriate stem cells to develop a single type of organoid with both chondrogenic and osteogenic differentiation capabilities, and by providing a suitable microenvironment for directed differentiation, it is possible to simplify the complex process of regenerating heterogeneous osteochondral tissues. Additionally, introducing induction methods that more closely mimic the natural microenvironment may simultaneously resolve the scientific challenges of gradient biomimicry in osteochondral regeneration.

Bone mesenchymal stem cells (BMSCs), with their dual differentiation potential into chondrocytes and osteoblasts [19], provide a promising solution for constructing gradient osteochondral tissues. Recent studies have demonstrated the feasibility of using BMSCs to regenerate both cartilage and bone, highlighting their potential for OCD repair [20]. Constructing BMSC-based organoids holds the promise of simultaneously repairing cartilage and subchondral bone injuries while markedly enhancing gradient biomimetic structures. However, to achieve this vision, it is essential to identify a suitable gradient biomimetic microenvironment that matches the natural gradient structure, ensuring that the induction process can genuinely accommodate individual variability.

A gradient microenvironment transitioning from low vascularization and hypoxia to high vascularization and ample oxygenation may represent the essential biomimetic environment we require. In the case of cartilage tissue, its inherent avascularity allows it to maintain a hypoxic state, which is crucial for the homeostasis of chondrocytes [21, 22]. Consequently, this hypoxic environment may serve as a critical inductive microenvironment for constructing cartilage organoids. A calcified interface layer was developed to prevent vascular invasion from the subchondral bone layer into the cartilage, thereby reducing endochondral ossification within the cartilage and promoting osteochondral regeneration [23]. Similarly, mesenchymal stem cells (MSCs) were preconditioned under hypoxic conditions, significantly enhancing their proliferation, migration, and matrix deposition capabilities *in vitro* [24]. A composite scaffold of slow-releasing PLGA microspheres and PLLA nanofibers was engineered to simulate a 3D hypoxic microenvironment, successfully facilitating the regeneration of cartilage

tissue from BMSCs [25]. Additionally, 3D-printed biological scaffolds were utilized to induce MSCs to construct high-quality transparent cartilage under hypoxic conditions [26]. These studies collectively confirm the pivotal role of a hypoxic microenvironment in the construction of cartilage organoids.

In contrast to cartilage, subchondral bone is a highly vascularized organ where angiogenesis plays a crucial role in osteogenesis. Enhanced angiogenesis in animal models has been shown to promote bone regeneration effectively [27, 28]. For example, 3D-printed biological scaffolds were modified with EPLQLKM and SVVYGLR peptides to impart pro-angiogenic properties, thereby enhancing BMSC-mediated osteogenic repair of osteoporotic bone defects [29]. This directly validates the importance of vascularization as a critical microenvironment for bone organoid ossification. Moreover, recent findings demonstrated that Notch1 signaling downregulates SRY-box transcription factor 9 (Sox9) and upregulates VEGFA expression, promoting angiogenesis and successfully guiding the endochondral ossification process within cartilage [30]. This further underscores the significance of a vascularized microenvironment in the construction of bone organoids from another perspective.

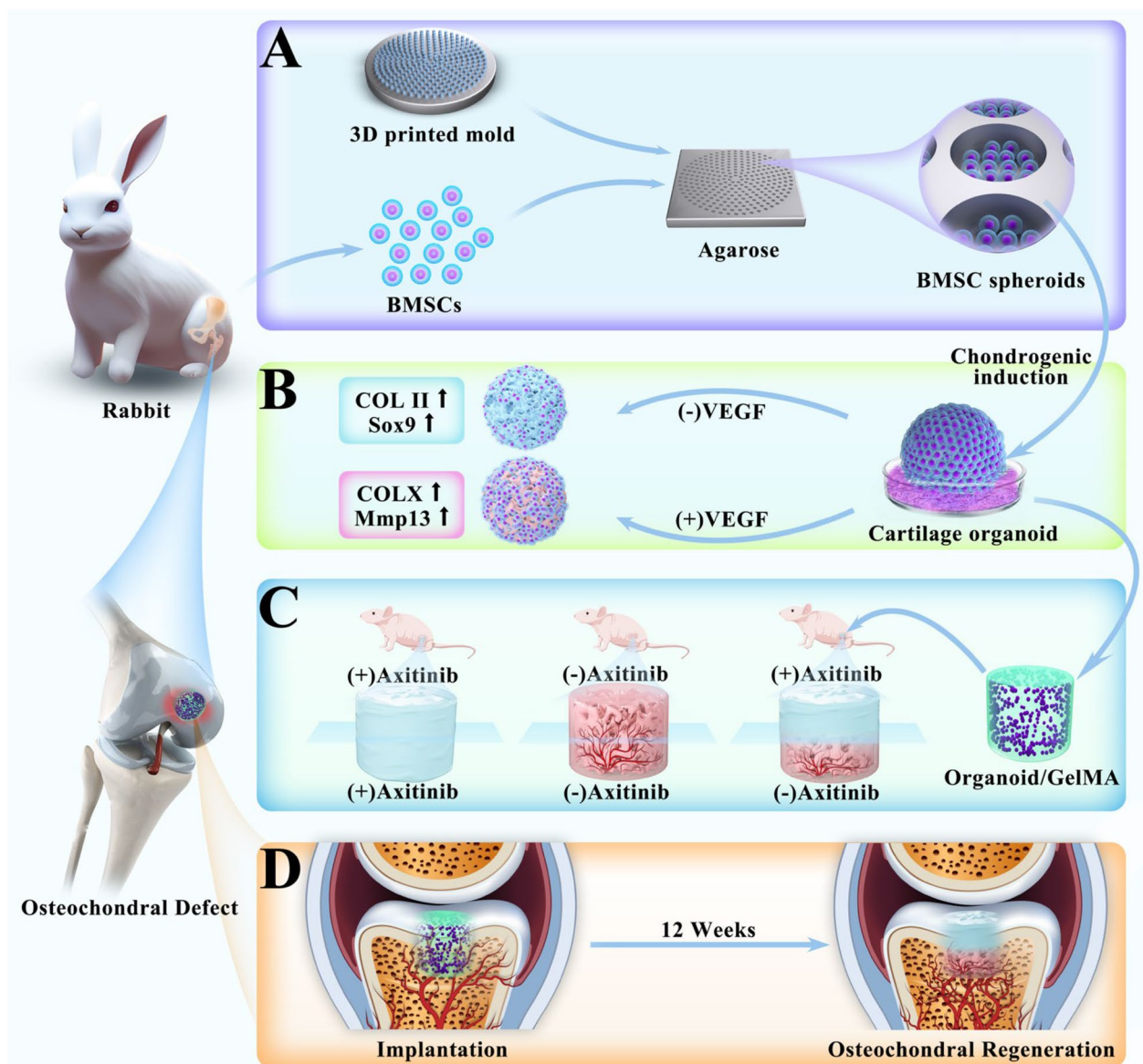
In natural joints, the transition from cartilage to subchondral bone involves a gradient change from avascular hypoxia to well-vascularized oxygenation. This gradient alteration in the microenvironment may be key to inducing BMSC-based organoids to form gradient osteochondral heterogeneous biomimetic structures. Therefore, this study aims to preconstruct a cartilage organoid based on BMSCs *in vitro*, which can regenerate a matching gradient heterogeneous biomimetic structure from cartilage to subchondral bone within a gradient microenvironment ranging from avascular to highly vascularized at OCD sites. This research uniquely proposes the use of natural gradient microenvironment to construct gradient heterogeneous biomimetic structures, providing a novel guidance direction for the clinical repair of OCDs (Scheme 1).

## Materials and methods

### Isolation, identification, and differentiation evaluation of rabbit BMSCs

#### Isolation of BMSCs

Eighteen 6-month-old New Zealand white rabbits (purchased from Yunde Biotechnology Co., Ltd.) weighing 3.0–3.5 kg were intravenously anesthetized. The surgical area was shaved and disinfected before performing bone marrow aspiration to collect 3 mL of iliac bone marrow using a syringe preloaded with 2 mL of heparin. The collected marrow was transferred to a 10 mL centrifuge tube, mixed with 3 mL of phosphate-buffered



**Scheme 1** Schematic Flowchart of Experimental Design. **a** Pre-quantified BMSCs were seeded into customized agarose wells for in vitro cultivation of BMSC spheroids. **b** Cartilage organoids were generated through in vitro chondrogenic culture of BMSC spheroids. Notably, cartilage organoids without VEGF addition retain chondrogenic induction, whereas cocultured with VEGF present hypertrophic tendency. **c** The in vitro cultured cartilage organoids were encapsulated into GelMA to prepare organoid/GelMA complexes. Subcutaneous implantation of these complexes supported bone formation in the subcutaneous vascular niche without Axitinib, while guiding cartilage regeneration at Axitinib created avascular microenvironment. **d** Organoid/GelMA complexes facilitated separately cartilage and subchondral bone formation due to the natural avascular microenvironment in the upper layer and the blood-rich microenvironment in the sublayer, giving rise to gradient heterogeneous osteochondral regeneration of in a rabbit OCD model

saline (PBS, Gibco, USA), and centrifuged at 1000 rpm for 10 min. The supernatant and fat layer were discarded, and the cells were washed twice with 3 mL PBS under the same centrifugation conditions.

The extracted cells were resuspended in low-glucose Dulbecco's Modified Eagle Medium (LG-DMEM, Gibco, USA) containing 10% fetal bovine serum (FBS, Gibco,

USA) and 1% penicillin–streptomycin. They were then seeded at a density of  $1.4 \times 10^4$  cells/mL in culture flasks and incubated at 37 °C with 5% CO<sub>2</sub>. The culture medium was replaced every 2–3 days. When cells reached 80–85% confluency, they were digested with trypsin and passaged at a 1:2 ratio. The same method was applied for subsequent passages. The growth of primary (P0) BMSCs was

observed from days 3–12 under a light microscope, and the morphology of second through sixth-passaged cells (P2–P6) was evaluated using phalloidin staining (No. C2201S, Beyotime, China) under a confocal microscope.

#### **Identification of BMSCs**

The surface markers CD29 and CD44 (MSC-related), as well as CD34 and CD45 (hematopoietic-related), were analyzed by flow cytometry and immunofluorescence staining in passaged BMSCs (P0, P1, P3, P5, and P7).

For flow cytometry, BMSCs at 80% confluency were digested with 1 mL of 0.25% trypsin and neutralized with 4 mL of LG-DMEM containing 10% FBS. The cell suspension was pipetted to ensure uniformity, and the density was adjusted to  $2 \times 10^5$  cells/mL. A 1 mL aliquot was transferred to 15 mL centrifuge tubes, centrifuged at 1200 rpm for 5 min, and the supernatant discarded. The BMSCs were washed with 1 mL of 5% bovine serum albumin (BSA, Gibco, USA) solution, centrifuged again, and resuspended in 100  $\mu$ L of 5% BSA. The suspension was divided into five groups and incubated overnight at 4 °C with the corresponding antibodies (Table S1, Supplemental Information): anti-CD29, anti-CD44, anti-CD34, anti-CD45, and a blank control. The following day, the cells were washed with 1 mL of 5% BSA, centrifuged, and resuspended in 500  $\mu$ L of 0.1 mol/L PBS. Analysis was performed using a Cytomics FC500 (Beckman Coulter, Miami, FL, USA) or Accuri C6 Plus (BD Biosciences, San Jose, CA, USA) and Csampl software ( $n=5$ ).

For immunofluorescence staining, cell slides were prepared by coating glass slides with poly-L-lysine for 120 min, followed by air-drying and sterilization under ultraviolet (UV) light for 1 h. Slides were placed into culture plate wells to facilitate cell attachment. Cells were fixed with 4% paraformaldehyde for 10 min, washed three times with PBS, and subjected to antigen retrieval in alkaline urea buffer at 95 °C for 10 min. After cooling, cells were permeabilized with 0.1% Triton X-100 for 10 min, washed with PBS, and blocked. Primary antibodies for CD29, CD44, CD34, and CD45 (Table S2, Supplemental Information) were incubated overnight at 4 °C. After washing with PBST, secondary antibodies (Table S2, Supplemental Information) were applied, followed by nuclear staining with 4',6-diamidino-2-phenylindole diacetate (DAPI, No. HY-D1738, MedChemExpress, USA). The slides were mounted with anti-fade reagent and observed under a confocal microscope. The relative expression levels of CD29, CD44, CD34, and CD45 at various passages were quantified using ImageJ software.

#### **Differentiation potential evaluation of passaged BMSCs**

The differentiation potential of BMSCs was assessed through osteogenic and chondrogenic induction.

Passaged BMSCs (P0, P1, P3, P5, and P7) at 70% confluency were cultured in osteogenic medium (LG-DMEM supplemented with 10% FBS, 50  $\mu$ M  $\alpha$ -ascorbate-2-phosphate, 10 mM  $\beta$ -glycerophosphate, and 0.1  $\mu$ M dexamethasone) or chondrogenic medium (LG-DMEM supplemented with 1% antibiotic–antimycotic,  $1 \times 10^{-3}$  M ascorbate-2-phosphate,  $100 \times 10^{-9}$  M dexamethasone, 40  $\mu$ g/mL proline, insulin–transferrin–sodium selenite premix, 6.25  $\mu$ g/mL insulin, 6.25  $\mu$ g/mL transferrin, 6.25  $\mu$ g/mL sodium selenite, 1.25  $\mu$ g/mL BSA, 5.35  $\mu$ g/mL linoleic acid, 100 ng/mL growth differentiation factor 5, and 10 ng/mL transforming growth factor beta-3). Half of the medium was replaced every 2–3 days.

Dual-lineage differentiation of BMSCs (P0–P7) was performed using: (i) Alizarin Red S staining to evaluate osteogenic potential and (ii) Alcian Blue staining to assess chondrogenic potential.

For Alizarin Red S staining (No. C0138, Beyotime, China), passaged BMSCs were incubated with the staining solution for 30 min at 37 °C, rinsed with distilled water, and imaged under a light microscope. For Alcian Blue staining (No. C0153S, Beyotime, China), BMSC slides were prepared, fixed, and stained with Alcian Blue solution for 30 min. After rinsing under running water and washing with PBS, slides were dehydrated, mounted, and imaged. The intensity of staining was quantified using ImageJ software.

#### **Development of cartilage organoids using P3 BMSCs**

##### **Preparation of organoid mold**

A 25,000 DPI photo-plotting printer (Koenen, Germany) was employed to fabricate polydimethylsiloxane (PDMS) master molds (Sylgard 184, Dow Corning, USA), containing cylindrical arrays with diameters of 200  $\mu$ m, depths of 150  $\mu$ m, and inter-cylinder spacings of 100  $\mu$ m. Subsequently, 3% (w/v) agarose (Invitrogen, China) was poured into the molds. Upon solidification, agarose replicas, approximately 1.8 cm<sup>2</sup> in area, were carefully punched out and placed into 24-well plates. The PDMS mold and agarose gel replica were photographed and documented. Following this, the agarose gel replicas were freeze-dried and analyzed using Scanning Electron Microscopy (SEM, FEI Inspect F50, USA). Each well was then filled with 1 mL of PBS and sterilized under UV light for 30 min. Each agarose gel replica contained approximately 2000 microwells, which served as inserts for high-throughput BMSC spheroid culture.

##### **Development of cartilage organoids**

P3 BMSCs, expanded in LG-DMEM containing 10% FBS, were used for cartilage organoid development. The BMSCs were harvested and seeded into each well of a 24-well plate (pre-loaded with agarose microwells) at a

density of  $1 \times 10^6$  cells per well. After self-aggregation, approximately 500 BMSCs were present per microwell. The BMSC spheroids were induced using the previously described chondrogenic medium, with half of the medium replaced every 2–3 days.

After 7 days, the BMSC spheroids were transferred to 96-well plates for further cartilage organoid development over an additional 21 days. This organoid preparation method was defined as 3D culture. As a control, P3 BMSCs were cultured on flat culture dishes with the same chondrogenic medium, referred to as 2D culture. Photographs were taken at different time points throughout the 28-day culture period using a light microscope.

To assess BMSC proliferation under 2D and 3D conditions on days 1, 3, 7, and 14, live/dead staining (Invitrogen, USA) was performed to investigate cell survival, and a cell counting kit-8 (CKK-8, No. C0041, Beyotime, China) was used to measure cell viability [31]. Phalloidin staining (No. C2203S, Beyotime, China) was applied to visualize the cell cytoskeleton. Chondrogenic differentiation was evaluated by immunofluorescence staining for aggrecan, Sox9, and COL II in BMSCs derived from both 3D organoid and 2D cultures (Table S2, Supplemental Information). Quantitative analysis of DNA, COL II, and glycosaminoglycan (GAG) content was conducted as previously described [32], with results expressed as COL II/DNA and GAG/DNA ratios.

#### **Chondrogenic evaluation of cartilage organoids**

To confirm the successful development of cartilage organoids, hematoxylin and eosin (H&E, No. C0105S, Beyotime, China) staining was performed. Briefly, organoids were fixed, dehydrated, and sectioned. After rehydration through graded ethanol, the sections were stained with hematoxylin and eosin, followed by mounting for structural observation and imaging. Safranin O/Fast Green (Saf-O/FG) staining (No. C0621S, Beyotime, China) was also performed. Sections were stained with Fast Green for 5 min, rinsed with tap water, differentiated in acetic acid for 30 s, washed, and stained with Safranin O for 8 min. After rapid dehydration with absolute ethanol, the sections were mounted and analyzed.

Additionally, immunofluorescence staining for COL II and aggrecan (Table S2, Supplemental Information) was conducted on organoid sections. Following rehydration, antigen retrieval, antibody incubation, and DAPI staining were performed as described in Sect. "Identification of BMSCs". The slides were mounted, and images were acquired for analysis. Finally, COL II and GAG content were measured at different time points to further evaluate chondrogenic protein expression.

#### **In vitro differentiation evaluation of cartilage organoids in avascular and vascular microenvironments**

##### ***In vitro incubation of cartilage organoids in avascular and vascular microenvironments***

Cartilage organoids, after 28 days of chondrogenic culture, were subjected to either a vascular (with vascular endothelial growth factor, VEGF) or avascular (without VEGF) medium for further chondrogenic and hypertrophic evaluation. Organoids were divided into three groups ( $n=5$ ): (-)VEGF, (+)VEGF, and Control. The (-) VEGF group was induced using the previously described chondrogenic medium, while the (+)VEGF group was treated with the same medium supplemented with VEGF (5 ng/mL, No. GMP-VE5H23, ACROBiosystems, USA). The Control group consisted of cartilage organoids collected after 28 days of chondrogenic culture, prior to further induction (without VEGF treatment). Half of the medium was replaced every 2–3 days. After 4 weeks of induction, cartilage organoids from all groups were collected for analysis.

##### ***Hypertrophic differentiation of cartilage organoids with VEGF treatment***

For quantitative real-time polymerase chain reaction (qPCR) analysis, total mRNA was extracted and purified from the induced cartilage organoids using Trizol reagent (Thermo Fisher Scientific, USA) [33]. The quantity and quality of the mRNA were determined by measuring absorbance at 260 nm with a NanoDrop 2000 spectrophotometer (Thermo Scientific, Wilmington, DE, USA). cDNA was synthesized from 1  $\mu$ g of mRNA using the Maxime RT PreMix kit (Intron Biotechnology, Seoul, Korea) in a Bio-Rad Thermocycler (Bio-Rad Laboratories, Hercules, CA, USA). For amplification, a 10  $\mu$ L reaction system was prepared with 5  $\mu$ L SYBR Green PCR Premix (Roche, Switzerland), 2  $\mu$ L RNA-free water, 2  $\mu$ L primers, and 1  $\mu$ L cDNA. The mixture was placed in a qPCR system and subjected to the following thermal cycling conditions: 95 °C for 10 min (denaturation); 40 cycles of 95 °C for 15 s (annealing) and 60 °C for 1 min (extension); followed by a melting curve from 60 °C to 95 °C, with 0.5 °C increments every 5 s. Primer sequences are listed in Table S3 (Supplemental Information). The relative fold changes in gene expression for the (+)VEGF and (-)VEGF groups were normalized to the Control group.

To further assess hypertrophic differentiation in VEGF-treated cartilage organoids, western blotting was performed [34]. Cartilage organoids were lysed on ice for 30 min using RIPA buffer (50 mM Tris-HCl pH 8.0, 150 mM NaCl, 1% Triton X-100, 100  $\mu$ g/mL PMSE, and a protease inhibitor cocktail). The lysates were clarified by centrifugation at 12,000 rpm for 20 min at 4 °C,

and protein concentrations were measured using a BCA assay. Equal amounts of protein (20  $\mu\text{g}$ ) were loaded onto 10% SDS-PAGE gels for electrophoresis and transferred to PVDF membranes. The membranes were blocked with 5% non-fat milk for 1 h at room temperature and incubated overnight at 4  $^{\circ}\text{C}$  with primary antibodies (Table S2, Supplemental Information). HRP-conjugated secondary antibodies (Table S2, Supplemental Information) were incubated for 2 h at room temperature. Enhanced chemiluminescence detection was used to visualize the blots, and quantitative analysis was performed using ImageJ software to evaluate target protein expression levels.

To validate differentiation outcomes, immunofluorescence staining was conducted to analyze the expression of chondrogenic proteins (COL II and GAG) and hypertrophic proteins (Matrix metalloproteinase-13 (Mmp13) and collagen type X (COL X)). The staining procedure followed the protocol described in Sect. "Identification of BMSCs". Quantitative analysis of fluorescence intensity was performed to assess differentiation.

#### **Genomic analysis of cartilage organoids in avascular and vascular microenvironments**

RNA sequencing was performed on cartilage organoids treated with or without VEGF using standard sequencing procedures provided by Cloud-seq Company, China [35]. A gene was considered expressed in a sample if its expression value was  $\geq 1$ . Differentially expressed genes were identified with a fold change of  $\geq 4$  and a  $p$ -value of  $\leq 0.05$ . Gene Ontology (GO) and Kyoto Encyclopedia of Genes and Genomes (KEGG) analyses were conducted using DAVID and REVIGO (<https://david.ncifcrf.gov>; <http://revigo.irb.hr/>). Target gene screening was performed using the GeneCards database (<https://www.genecards.org/>). For each group, three biological replicates were collected, and their RNA was extracted, sequenced, and analyzed.

#### **In vivo cartilage and bone regeneration of Organoid/GelMA complexes in avascular and vascular microenvironments**

##### **Preparation of double-layer organoid/GelMA complexes with or without axitinib**

The gelatin methacryloyl (GelMA, No. LBH020001, Lab of Health, China) precursor solution was prepared by dissolving GelMA (pre-loaded with the blue light initiator lithium phenyl-2,4,6-trimethylbenzoylphosphinate) in PBS to a final concentration of 0.15 g/mL. To prepare the organoid/GelMA complexes, induced cartilage organoids were suspended in the GelMA precursor solution at a 1:1 volume ratio. To create an avascular microenvironment, the anti-angiogenic drug Axitinib (No. HY-10065,

MedChemExpress, USA) was added to the organoid/GelMA complex at a final concentration of 0.40 nM, designated as the (+)Axitinib layer solution. The vascular group did not include Axitinib and was designated as the (-)Axitinib layer solution. These two solutions were transferred to cylindrical molds with a diameter of 4 mm and height of 1.5 mm, and solidified after 15 s of exposure to Blu-ray light (wavelength 405 nm), resulting in two types of cylinders. These cylinders were then stacked to form a double-layer cylinder with an overall diameter of 4 mm and a height of 3 mm, yielding three experimental groups: (+)Axitinib/(+)Axitinib, (-)Axitinib/(-)Axitinib, and (+)Axitinib/(-)Axitinib.

##### **Cartilage and bone regeneration of organoid/GelMA complexes in avascular and vascular microenvironments in a nude mouse model**

Six-week-old female nude mice ( $n=5$ ) were purchased from Shanghai SLAC Laboratory Animal Co., Ltd. The double-layer organoid/GelMA complexes from each group were subcutaneously implanted into the dorsal region of the mice. After 4 weeks, the mice were euthanized under deep anesthesia, and the regenerated tissues were harvested for analysis.

Micro-computed tomography (Micro-CT) was used to evaluate the osseous characteristics of the double-layer organoid/GelMA complexes after subcutaneous implantation. The regenerated tissues were fixed in 4% paraformaldehyde, then scanned at 40 kV, 600  $\mu\text{A}$ , and a resolution of 8.75  $\mu\text{m}$  using the Skyscan 1176 Micro-CT system (Bruker, Germany). The images were reconstructed with a dynamic range of 0–0.16, a beam hardening setting of 20, and a ring artifact correction of 10. 3D reconstructions were generated using CTvox software (Bruker, Germany). To quantify osseous features, the region of interest (ROI) was defined using CTAnalyser software (Bruker, Germany), and key parameters, including trabecular number (Tb.N) and trabecular thickness (Tb.Th), were calculated within the ROI ( $n=3$ ). These analyses provided quantitative metrics for evaluating the osseous ECM deposition of the organoid/GelMA complexes.

The harvested tissues were sectioned for histological analysis, including H&E and Saf-O/FG staining. Briefly, tissues were fixed in 4% paraformaldehyde for 24 h, decalcified in 10% ethylenediamine tetraacetic acid (ChelatoCal, National Diagnostics, Atlanta, GA, USA) for 4 weeks, then dehydrated, embedded, and sectioned. H&E and Saf-O/FG staining were performed to assess the chondrogenic and osteogenic potential of the regenerated tissues. Quantification of COL II and GAG content was performed as described in Sect. "Development of cartilage organoids".

To evaluate the effect of the vascular microenvironment on cartilage and bone regeneration, CD31 immunofluorescence staining was performed on tissue sections. Semi-quantitative analysis of CD31 expression followed the protocol outlined in Sect. "[Development of cartilage organoids](#)", using antibodies listed in Table S2 (Supplemental Information).

### **Gradient heterogeneous osteochondral regeneration of organoid/GelMA cylinder in a rabbit OCD model**

#### ***Preparation of intact organoid/GelMA cylinder***

To prepare an intact organoid/GelMA cylinder, the GelMA precursor solution, with cartilage organoids added, was transferred into a cylindrical mold (4 mm diameter, 3 mm height). The mixture was fully solidified after 30 s of exposure to Blu-ray light (wavelength 405 nm). A pure GelMA cylinder of the same size as the organoid/GelMA cylinder was also prepared as a control.

#### ***Implantation of organoid/GelMA cylinder in a rabbit OCD model***

A full-thickness OCD model was created in adult male New Zealand white rabbits. The rabbits were sedated with Zoletil50 (0.35 mL/kg, Virbac, France), and preoperative antibiotics (10 mg/kg, Baytril, Bayer Korea) and analgesics (5 mg/kg, Tramadol HCl, HanAll Biopharma, Korea) were administered subcutaneously to prevent complications. A lateral parapatellar approach was used to expose the patellar groove, with sequential incisions through the skin, subcutaneous tissue, and joint capsule. The patella was dislocated medially to reveal the trochlear groove. A 4-mm diameter cylindrical defect, 3 mm in depth, was created in the femoral trochlea using a high-speed drill (Colibri II, Depuy Synthes, Oberdorf, Switzerland).

The rabbits were randomly divided into three groups: the empty group, the GelMA group, and the organoid/GelMA group (n=6). The defect sites were implanted with either a GelMA cylinder or an autologous organoid/GelMA cylinder, while the empty group received no implant. The joint capsule and subcutaneous tissue were sutured with absorbable sutures, and the skin was closed with nylon sutures. Postoperative care involved 7 days of monitoring, with the surgical site disinfected with chlorhexidine and antibiotics and analgesics administered subcutaneously. The rabbits were housed for 12 weeks post-surgery. At the endpoint, the rabbits were euthanized under deep anesthesia (5 MAC isoflurane) and intravenous KCl (150 mg/kg). The repaired knee joints were harvested, photographed, and fixed in 4% paraformaldehyde for further analysis.

### ***Evaluation of gradient heterogeneous osteochondral tissue regeneration***

Regenerated tissue was assessed using the International Cartilage Repair Society (ICRS) scoring system (Table S4, Supplemental Information). Final scores were determined by averaging the results from five independent researchers (n=5).

Micro-CT analysis was performed on the repaired joint tissue to obtain 2D and 3D images. Parameters were set at 40 kV, 600  $\mu$ A, and a resolution of 8.75  $\mu$ m. Tb.Th and bone volume fraction (BV/TV) were quantified within the region of interest (ROI) using CTAnalyser software, as described in Sect. "[Cartilage and bone regeneration of organoid/GelMA complexes in avascular and vascular microenvironments in a nude mouse model](#)".

Histological analyses were conducted to evaluate cartilage and subchondral bone regeneration in the knee joint. Tissue sections were stained with H&E and Saf-O/FG. For toluidine blue staining (No. HY-D0220, Med-ChemExpress, USA), hydrated sections were incubated with toluidine blue staining solution at room temperature for 30 min, followed by differentiation in 1% hydrochloric acid-alcohol and further rinsing. Sections were then dehydrated and mounted for observation. Immunohistochemical staining for COL II was performed to confirm cartilage formation. After rehydration, antigen retrieval was conducted using an alkaline urea buffer. Permeabilization was done with 0.1% Triton X-100 in PBS, followed by blocking. Sections were incubated with primary and secondary antibodies (Table S2, Supplemental Information). DAB staining (No. P0203, Beyotime, China) was used for visualization, followed by hematoxylin counterstaining and mounting. Results were imaged and semi-quantitatively analyzed.

#### ***Biosafety assessment***

To assess the biosafety of the organoid/GelMA cylinder, tissue samples from the heart, liver, spleen, lungs, and kidneys were collected from treated rabbits for histological analysis (n=5). Abdominal aortic blood was also collected for complete blood count and liver and kidney function tests (n=5) to evaluate systemic biosafety.

#### ***Statistical analysis***

Statistical analysis was performed using SPSS software (Version 22.0, SPSS Inc., USA), ImageJ software (Version 1.8.0, National Institutes of Health, USA), and GraphPad Prism (Version 9.0, GraphPad Software Inc., USA). All data are presented as mean  $\pm$  standard deviation (SD) and were derived from at least three independent experiments. For two-group comparisons, the Student's *t*-test

was used. For multi-group comparisons, one-way analysis of variance (ANOVA) was conducted. A *p*-value of less than 0.05 was considered statistically significant.

## Results and discussion

### Isolation, identification, and differentiation evaluation of rabbit BMSCs

The morphology of P0 BMSCs was observed under a light microscope. Adherent BMSCs primarily exhibited triangular, spindle-shaped, or fusiform morphologies. By day 3 of culture, the BMSCs adhered to the bottom of the culture flask and gradually became denser and more uniform in appearance. By day 5, the BMSCs had reached confluence and completely covered the bottom of the culture dish by day 12 (Fig. 1a).

Passaged BMSCs from P2 to P6 were subjected to phalloidin staining. The results showed that P2 and P3 BMSCs exhibited uniform cytoskeleton morphologies and were well-stretched. In contrast, P4 BMSCs began to exhibit signs of morphological shrinkage, and P5 and P6 BMSCs showed severe contraction (Fig. 1b).

Flow cytometry analysis of surface markers in passaged BMSCs revealed that MSC markers CD29 and CD44, initially high in P0 (71.9% and 98.4%, respectively), gradually decreased with increased passages, reaching their lowest levels at P7 (67.3% and 87.5%), though they remained relatively high throughout. In contrast, the hematopoietic markers CD34 and CD45, which were low in P0 (0.5% and 4.31%, respectively), further decreased to 0.36% and 0.29% at P7, maintaining negative results throughout. Notably, these markers showed significantly low expression already at P3 (0.4% and 0.7%, respectively) (Fig. 1c, d). Immunofluorescence staining confirmed these trends, with CD29 and CD44 gradually declining but remaining positive, while CD34 showed minimal fluorescence, and CD45 fluorescence almost completely disappeared by P3 (Fig. S1a, b, Supplemental Information).

The osteogenic and chondrogenic differentiation potential of BMSCs was assessed using Alizarin Red S and Alcian Blue staining. Alizarin Red S staining revealed clear orange-red calcium deposition in P0, P1, and P3 BMSCs (Fig. 1e, f). These regions significantly weakened, and the stained areas visibly shrank in P5 and P7 BMSCs. Similarly, Alcian Blue staining demonstrated substantial sulfated mucopolysaccharides in P0 and P1 BMSCs, with a significant decrease after P3. By P5 and P7, the stained areas were further reduced (Fig. 1g, h). These findings confirmed that passaged BMSCs possessed osteogenic and chondrogenic differentiation potential, though this ability declined after P3.

Maintaining BMSC viability and stemness under conventional culture conditions is critical for advancing the development of BMSC-derived organoids. Our

data suggest that BMSCs undergo a gradual decline in stemness with increased passaging, primarily due to cellular senescence, oxidative stress, and epigenetic changes. Telomere shortening and DNA damage during passaging lead to senescence [36], while the accumulation of reactive oxygen species damages cellular components and inhibits differentiation potential. Additionally, epigenetic modifications, such as DNA methylation and histone alterations, suppress the expression of stemness-related genes [37]. Metabolic shifts from glycolysis to mitochondrial oxidative phosphorylation also contribute to reduced stemness, as increased reactive oxygen species production accelerates aging [38].

Based on these findings, we concluded that at least three passages are required to eliminate hematopoietic cells during BMSC isolation. However, to obtain a sufficient quantity of BMSCs while maintaining their proliferative capacity, optimal cell morphology, and multi-lineage differentiation potential, only BMSCs before P3 should be used. Thus, P3 BMSCs were selected for subsequent cartilage organoid development.

### Development of cartilage organoids using passaged BMSCs

A photolithography technique was employed to design a cylindrical array on a silicon wafer, with each pillar having a diameter of 200  $\mu\text{m}$ , a depth of 150  $\mu\text{m}$ , and an inter-pillar spacing of 100  $\mu\text{m}$  (Fig. 2a). The cylindrical structures of the molds were clearly observed under both macroscopic and microscopic examination (Fig. 2b). Using this master mold, replicas were produced in 3% agarose, resulting in a non-adherent surface (Fig. S2a, Supplemental Information). Freeze-drying induced a morphological change, with the microcavities transitioning from a circular to a honeycomb-like shape; however, the distinct distribution of individual microcavities remained clearly visible (Fig. S2b, Supplemental Information). Each replica contained approximately 2000 microcavities, providing isolated growth spaces for the development of BMSC spheroids. The agarose gel replicas were subsequently transferred into wells of a 24-well plate, with the microcavities oriented upwards. Photographic documentation revealed that the agarose replicas faithfully replicated the shape of the PDMS mold, and both the PDMS mold and the replica fit well within the 24-well plate, preventing displacement during subsequent organoid culture (Fig. S2c, d, Supplemental Information).

A total of  $1 \times 10^6$  P3 BMSCs were seeded into each well of the 24-well plate, resulting in approximately 500 BMSCs per microcavity. The 150  $\mu\text{m}$  depth of the microcavities provided sufficient space for the formation of BMSC spheroids. After 7 days of culture in chondrogenic medium, the BMSC spheroids were individually

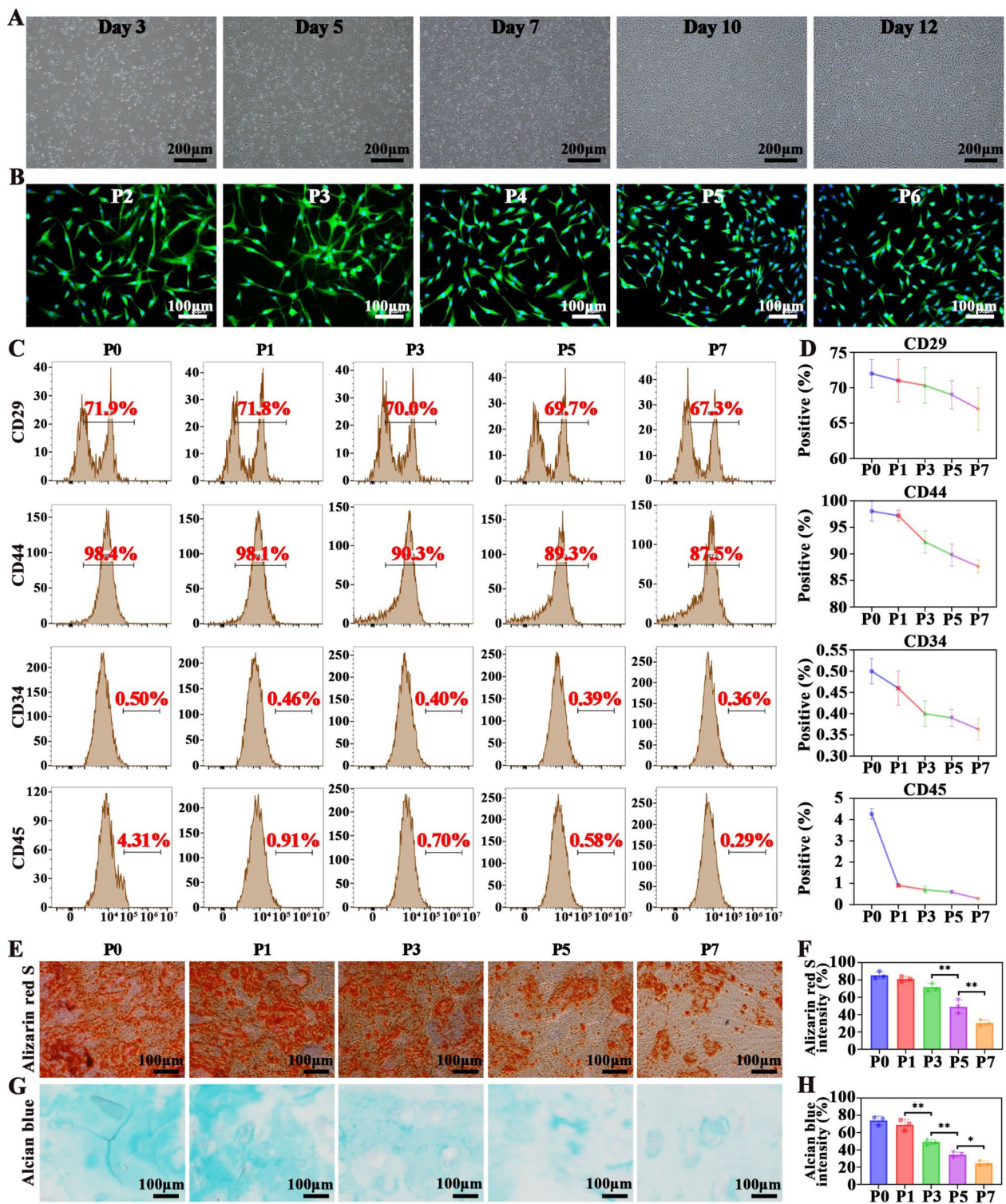


**Fig. 1** Isolation and Identification of Rabbit-derived BMSCs. **a** Morphological observation of P0 BMSCs cultured in vitro for 3, 5, 7, 10, and 12 days, visualized using a light microscope. **b** Morphology of passaged BMSCs from P2 to P6, imaged with a confocal microscope. **c** Flow cytometry analysis of BMSCs from P0 to P7, illustrating the expression of MSC surface markers CD29 and CD44, as well as hematopoietic marker CD34 and CD45. **d** Quantification of positive BMSCs percentages for surface marker CD29, CD44, CD34, and CD45 across P0 to P7. **e** Osteogenic differentiation of BMSCs from P0 to P7, determined by Alizarin Red S staining of mineralized ECM. **f** Quantification of Alizarin Red S intensities based on Alizarin Red S staining. **g** Chondrogenic differentiation of BMSCs from P0 to P7, determined by Alcian Blue staining of proteoglycans. **h** Quantification of Alcian Blue intensities based on Alcian Blue staining. n = 3; \*p < 0.05, \*\*p < 0.01

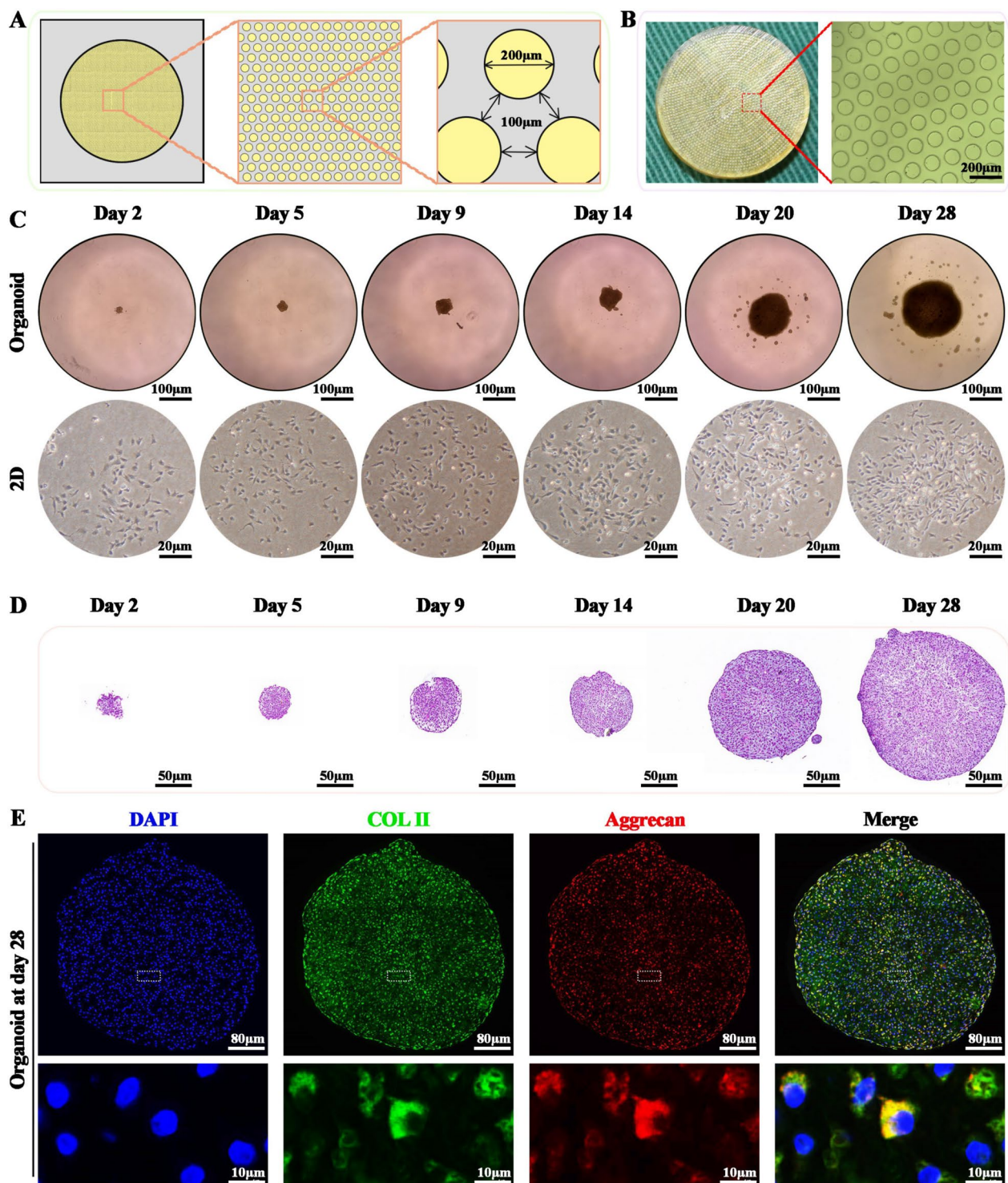


**Fig. 2** Development of Cartilage Organoids Using a High-Throughput Agarose Platform. **a** Schematic diagram of the mold design for high-throughput platform. **b** General appearance and its enlarged details of the high-throughput PDMS mold platform. **c** Compared to traditional 2D cultures in standard dishes, BMSCs self-assembled into cartilage organoids after 28 days of chondrogenic cultivation based on the agarose platform. **d** H&E staining images of cartilage organoids at 2, 5, 9, 14, 20, and 28 days of chondrogenic culture. **e** Representative immunofluorescence images showing COL II and aggrecan expression in cartilage organoids at 28 days. White dotted squares in the upper panel indicate regions that are enlarged in the lower panel for detailed visualization

transferred to a 96-well plate for an additional 21 days of chondrogenic culture.

Over the total 28-day chondrogenic culture, the 3D-cultured BMSC spheroids gradually developed into cartilage organoids, as observed under a light microscope (Fig. 2c). The diameter of the organoids increased progressively over time, from  $23.38 \pm 2.20 \mu\text{m}$  on day 2, to  $34.44 \pm 4.89 \mu\text{m}$  on day 5,  $58.90 \pm 38.99 \mu\text{m}$  on day 9,  $72.99 \pm 6.63 \mu\text{m}$  on day 14,  $138.05 \pm 32.86 \mu\text{m}$  on day 20, and  $190.29 \pm 29.17 \mu\text{m}$  on day 28 (Fig. S3, Supplemental Information). In contrast, while 2D-cultured BMSCs proliferated normally and eventually covered the surface of the culture dish, they failed to transition from a 2D structure into 3D spherical aggregates (Fig. 2c).

Cell viability and proliferation under 2D and 3D culture conditions were further investigated. Compared to the 3D culture, 2D-cultured BMSCs exhibited a higher percentage of dead cells, with the percentage increasing over time from days 1, 3, 7, and 14 (Fig. S4a, b, Supplemental Information). These results suggest that 3D culture effectively mitigates the cell damage associated with traditional 2D methods. Furthermore, CCK-8 assays revealed significantly higher proliferative activity in the 3D-cultured group compared to the 2D group (Fig. S4c, Supplemental Information), highlighting the superior ability of 3D culture to sustain cell proliferation.

Phalloidin staining revealed significant cytoskeletal morphological differences between the two groups [39]. In the 3D group, BMSCs exhibited elongated spindle shapes that were maintained up to day 14, whereas in the 2D group, the cytoskeleton gradually collapsed, with this phenomenon becoming more pronounced with prolonged culture (Fig. S4d, Supplemental Information). These findings confirm that 3D culture offers better support for BMSC proliferation and morphology compared to traditional 2D culture.

Immunofluorescence staining of BMSCs after 28 days of culture revealed significant positive expression of chondrogenic markers (aggrecan, Sox9, and COL II) in the 3D group, while these markers were nearly absent in the 2D group, indicating a lack of chondrogenic differentiation in the 2D group (Fig. S5a, Supplemental Information). Furthermore, BMSCs from the 3D-cultured organoids contained significantly higher levels of COL II/DNA and GAG/DNA compared to the 2D-cultured condition, further demonstrating the superiority of 3D culture in supporting chondrogenic differentiation and cartilage organoid formation (Fig. S5b, c, Supplemental Information).

Collectively, our data suggest that BMSCs in the 3D culture group exhibited superior proliferation, better cell morphology, and more stable maintenance of stemness, leading to the formation of favorable cartilage organoids

compared to the 2D culture. It has been observed before that BMSCs secrete a greater amount of ECM within the 3D space [40]. This increased ECM secretion provides favorable attachment sites for the cells, which may facilitate continued cell proliferation. Similarly, it was demonstrated that BMSC/scaffold-hydrogel complexes in 3D culture exhibited lower cell death and better maintenance of stem cell characteristics compared to 2D culture, which was identified as the reason why BMSCs in 2D culture failed to form organoid spheroids [41]. Additionally, BMSCs cultured under 2D conditions exhibited a typical single, dispersed morphology, while BMSCs under 3D culture conditions formed complex network structures and interacted with surrounding cells and the scaffold [42]. These differences explain why BMSCs in 2D culture fail to form organoids, which aligns with the current research trend towards tissue engineering and 3D organoid construction technologies that aim to transition MSCs from conventional 2D culture to more biomimetic 3D environments.

From a more intuitive standpoint, the transition from 2D planar culture to 3D spatial culture for BMSCs can be viewed as a process of establishing a more biomimetic living environment. In vivo, BMSCs naturally reside in a 3D physiological environment, where they are exposed to extensive cell–cell and cell–matrix interactions [43]. However, the isolation and culture of BMSCs on 2D surfaces disrupts this native microenvironment. The 2D culture conditions, which deviate significantly from the in vivo 3D environment, inevitably hinder the formation of cartilage-like organoids.

H&E staining of cartilage organoids at days 2–28 revealed circular sections consistent with the gross appearance observed under a light microscope. These sections suggested more densely packed cells and a more homogeneously distributed cartilage-like ECM with increasing culture duration (Fig. 2d). Saf-O/FG staining demonstrated that organoid size increased progressively over the 28-day culture period, consistent with H&E staining results (Fig. S6, Supplemental Information). The intensive deposition of chondroitin sulfate stained by Safranin O dye confirmed enhanced chondrogenic characteristics during this period [44]. After 28 days of 3D culture, BMSC-derived cartilage organoids were substantial and visible to the naked eye, appearing as spherical, opaque, white aggregates sedimented at the bottom of the 96-well plates (Fig. S7, Supplemental Information).

Immunofluorescence imaging further showed the gradual enlargement of cartilage organoids on days 9, 20, and 28, accompanied by increasing fluorescence intensity of chondrogenic markers (COL II and aggrecan). On day 9, COL II was nearly undetectable, and aggrecan exhibited weak fluorescence. Both markers displayed enhanced

fluorescence intensity from day 20 to day 28 (Fig. S8a, b, Supplemental Information; Fig. 2e). The results of Saf-O/FG staining and immunofluorescence were further corroborated by the quantification of GAG and COL II content, which showed an increasing trend with culture time (Fig. S9a, b, Supplemental Information). These findings validate the successful construction of cartilage organoids by day 28.

#### **In vitro differentiation evaluation of cartilage organoids in avascular versus vascular microenvironments**

To evaluate how a vascular microenvironment regulates the differentiation of cartilage organoids in vitro, VEGF was used for co-culturing the cartilage organoids obtained after 28 days of chondrogenic culture (Fig. 3a). Compared to the pre-induced control group (cartilage organoids after 28 days of culture), qPCR data indicated that after 4 weeks of co-culture with VEGF, the (-)VEGF group showed significantly increased expression of chondrogenic-related genes *Col2a1* ( $p < 0.001$ ) and *Sox9* ( $p < 0.001$ ), alongside decreased expression of hypertrophic-related genes *Col10a1* ( $p < 0.05$ ) and *Mmp13* ( $p < 0.05$ ). In contrast, the (+)VEGF group exhibited significantly higher expression of hypertrophic-related genes *Col10a1* ( $p < 0.001$ ) and *Mmp13* ( $p < 0.001$ ), but decreased expression of chondrogenic-related genes *Col2a1* ( $p < 0.01$ ) and *Sox9* ( $p < 0.001$ ) (Fig. 3b).

Western blot analysis further confirmed these findings, showing trends in protein levels consistent with the qPCR results for both chondrogenic and hypertrophic markers in the (+)VEGF group, when compared to the control group (Fig. 3c, d). Quantification of immunofluorescence staining revealed that the expression of chondrogenic markers COL II ( $p < 0.01$ ) and GAG ( $p < 0.01$ ) was significantly higher in the (-)VEGF group than in the (+)VEGF group. Conversely, hypertrophic markers *Mmp13* ( $p < 0.01$ ) and COL X ( $p < 0.001$ ) were significantly more expressed in the (+)VEGF group compared to the (-)VEGF group (Fig. 3e, f).

Considering that hypertrophic differentiation of BMSCs in cartilage organoids could eventually lead to endochondral ossification [3], these findings demonstrate that cartilage organoids possess bidirectional differentiation potential toward both chondrogenic and osteogenic lineages under VEGF treatment. This highlights their excellent stemness maintenance capability. Moreover, the avascular microenvironment facilitates chondrogenic differentiation, whereas the vascular niche guides osteogenic differentiation. In the natural anatomy of endochondral tissues, cartilage typically resides in an ischemic microenvironment, while bone tissue is associated with a vascular-rich environment. These results suggest that the natural gradient of the vascular microenvironment

in vivo could potentially drive the regeneration of both cartilage and bone tissues from a single cartilage organoid.

#### **Mechanistic study on the regulation of differentiation potential in cartilage organoids by the vascular microenvironment**

Whole RNA sequencing was performed on cartilage organoids at day 28 to explore the underlying mechanisms of VEGF signaling in inducing chondrogenic and osteogenic tendencies. The resulting volcano plot revealed that 41 genes were upregulated, and 12 genes were downregulated in the VEGF-treated group of cartilage organoids (Fig. 4a). Differential analysis of gene expression profiles between the (-)VEGF and (+)VEGF groups revealed significant differences (Fig. 4b). Specifically, genes associated with angiogenesis (e.g., *VEGFA*, *ANGPT1*, *NOTCH1*, *MMP9*, and *DLL4*), hypertrophy (e.g., *RUNX2*, *COL10A1*, *MMP13*, *OSTERIX*, and *COL1A1*), and osteogenesis (e.g., *BMP2*, *BGLAP*, *Osteopontin*, *CTNNA1*, and *DLX5*) were upregulated in the (+)VEGF group compared to the (-)VEGF group. In contrast, genes associated with chondrogenesis (e.g., *SOX9*, *COL2A1*, *ACAN*, *COMP*, and *PRG4*) were significantly downregulated in the (+)VEGF group compared to the (-)VEGF group (Fig. 4c). Detailed enrichment analysis of the differentially expressed genes further highlighted distinctive gene expression patterns related to angiogenesis, hypertrophy, osteogenesis, and chondrogenesis in the cartilage organoids treated with or without VEGF (Fig. S10a, d, Supplemental Information).

GO analysis revealed that upregulated genes in the (+)VEGF group were enriched in processes related to angiogenesis, hypertrophy, and osteogenesis (Fig. 4d), while downregulated genes were associated with chondrogenic differentiation (Fig. 4e). These biological pathways could be facilitated by VEGF-induced angiogenesis, hypertrophy, and osteogenesis. KEGG pathway analysis further indicated the activation of angiogenetic, hypertrophic, and osteogenic signaling pathways in the (+)VEGF group (Fig. 4f). Additionally, KEGG analysis revealed suppression of chondrogenic-related pathways, including TGF- $\beta$  signaling, Wnt signaling, and Hedgehog signaling, in the (+)VEGF group (Fig. 4g). Overall, our RNA sequencing data demonstrate that the addition of VEGF positively regulates cartilage organoid development by enhancing angiogenetic, hypertrophic, and osteogenic activities, while concurrently suppressing chondrogenesis.

#### **Evaluation of chondrogenic and osteogenic activities of organoid/GelMA complexes in vivo**

To validate the regulatory effects of vascular and avascular microenvironments on the differentiation of cartilage

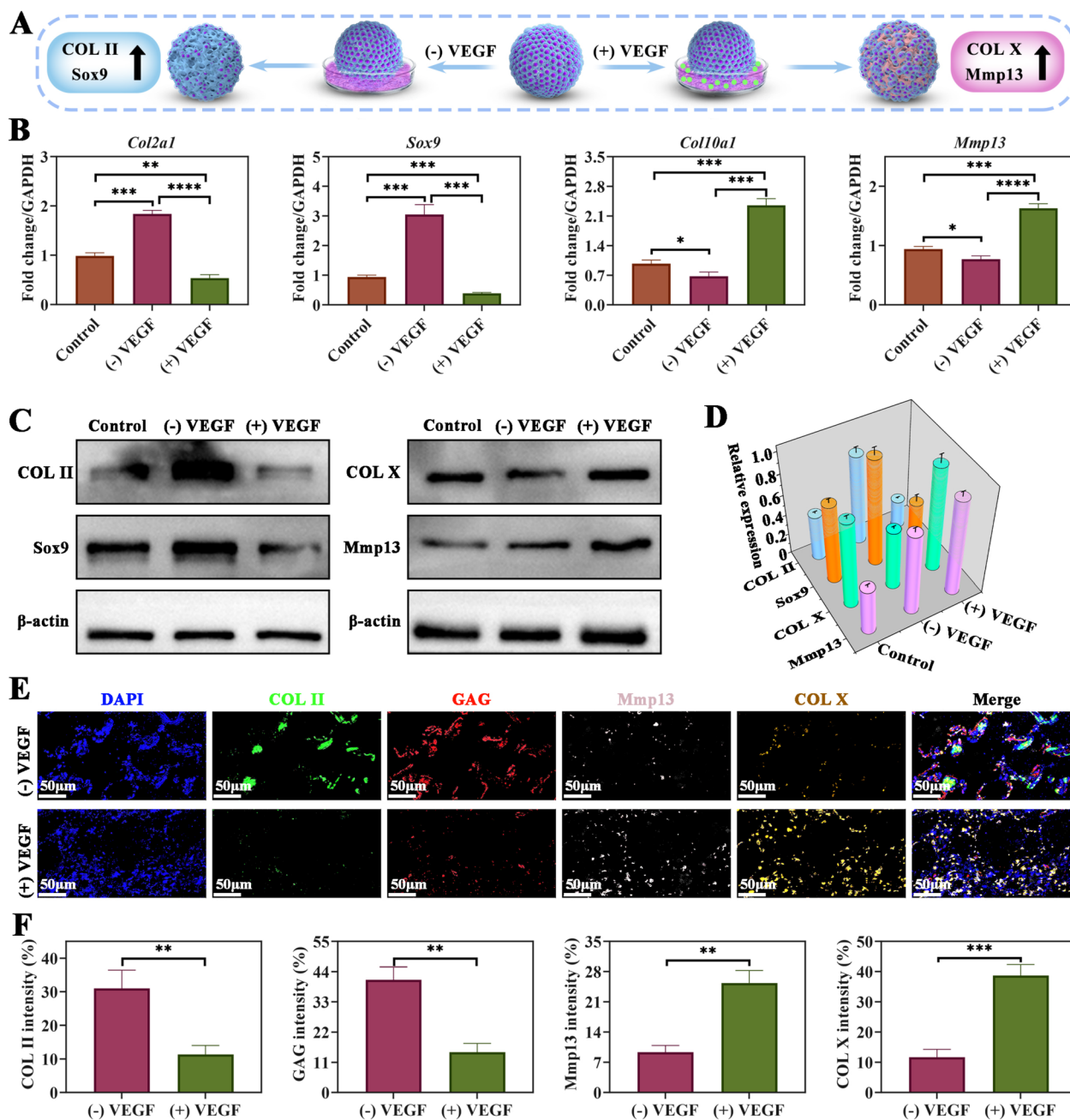


**Fig. 3** In Vitro Hypertrophic Potential of Cartilage Organoids in the Presence of VEGF. **a** Schematic illustrating that cartilage organoids maintain chondrogenesis without VEGF but shift toward osteogenesis with VEGF. **b** qPCR analysis of chondrogenic genes (*Col2a1* and *Sox9*) and hypertrophic genes (*Col10a1* and *Mmp13*) in cartilage organoids cocultured with or without VEGF for 4 weeks (control group: cartilage organoids before VEGF treatment). **c** Western blot analysis of chondrogenic proteins (COL II and Sox9) and hypertrophic proteins (COL X and Mmp13) in cartilage organoids cocultured with or without VEGF for 4 weeks (control group: cartilage organoids before VEGF treatment). **d** Quantitative analysis of COL II, Sox9, COL X, and Mmp13 protein levels from western blot images. **e** Immunofluorescence staining for COL II, GAG, Mmp13, and COL X in cartilage organoids cocultured with or without VEGF for 4 weeks. **f** Quantitative analysis of COL II, GAG, Mmp13, and COL X fluorescence intensities. n = 5; \*p < 0.05, \*\*p < 0.01, \*\*\*p < 0.001, \*\*\*\*p < 0.0001

organoids in vivo, double-layer organoid/GelMA complexes were subcutaneously implanted in nude mice (Fig. 5a). The subcutaneous environment, naturally rich

in vasculature, served as the vascular microenvironment, while the anti-angiogenic drug Axitinib was used to create an avascular niche. The mice were divided into three

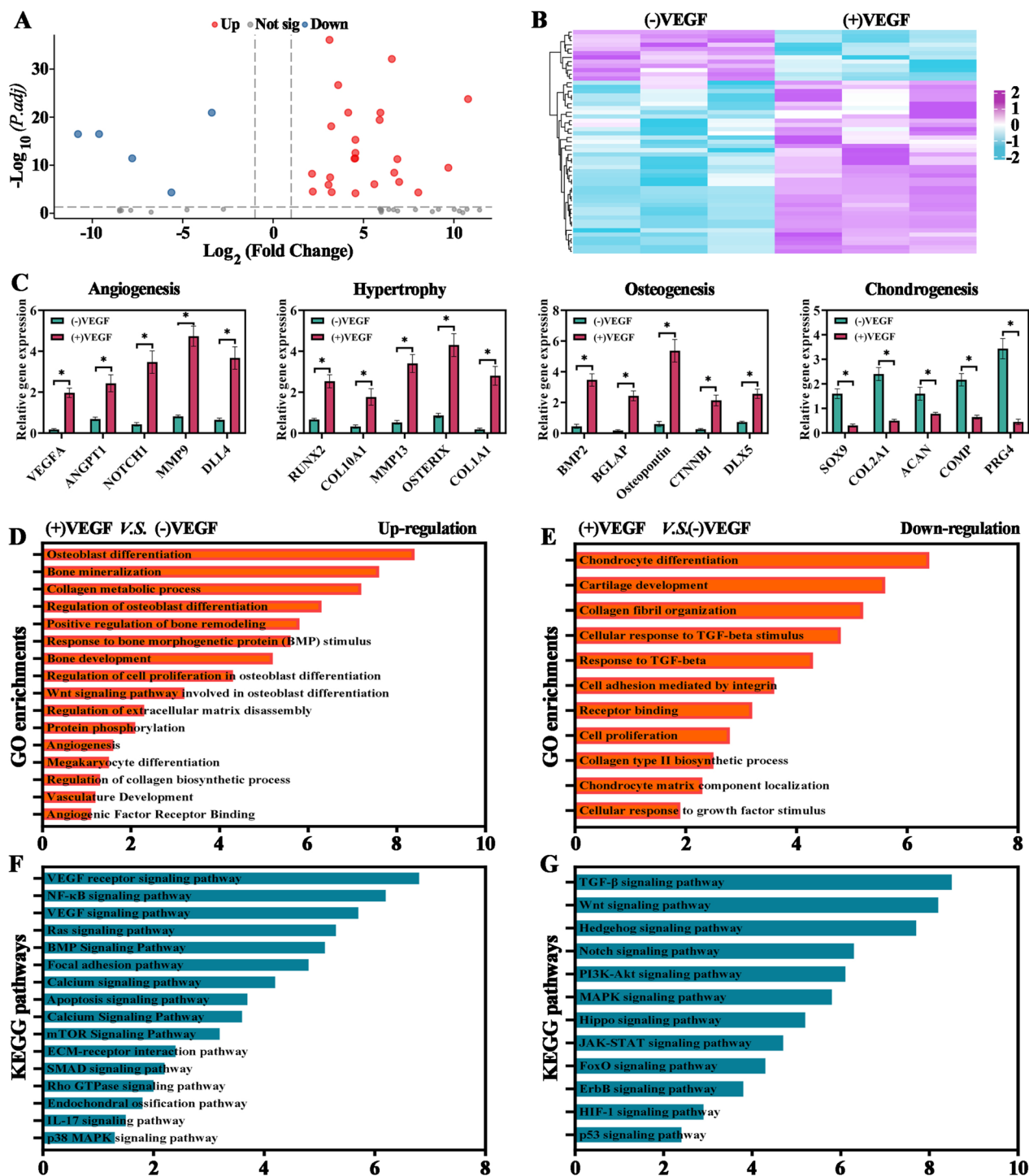


**Fig. 4** Whole Transcriptome RNA Sequencing Analysis for Cartilage Organoids in the Presence or Absence of VEGF In Vitro. **a** Volcano plot displaying upregulated and downregulated genes in cartilage organoids with or without VEGF treatment. **b** Heatmap illustrating the expression levels of these genes. **c** Relative expression of genes related to angiogenesis, hypertrophy, osteogenesis, and chondrogenesis in cartilage organoids with or without VEGF treatment. GO enrichment analyses of **d** upregulated genes and **e** downregulated genes. KEGG pathway enrichment analyses of **f** upregulated genes and **g** downregulated genes

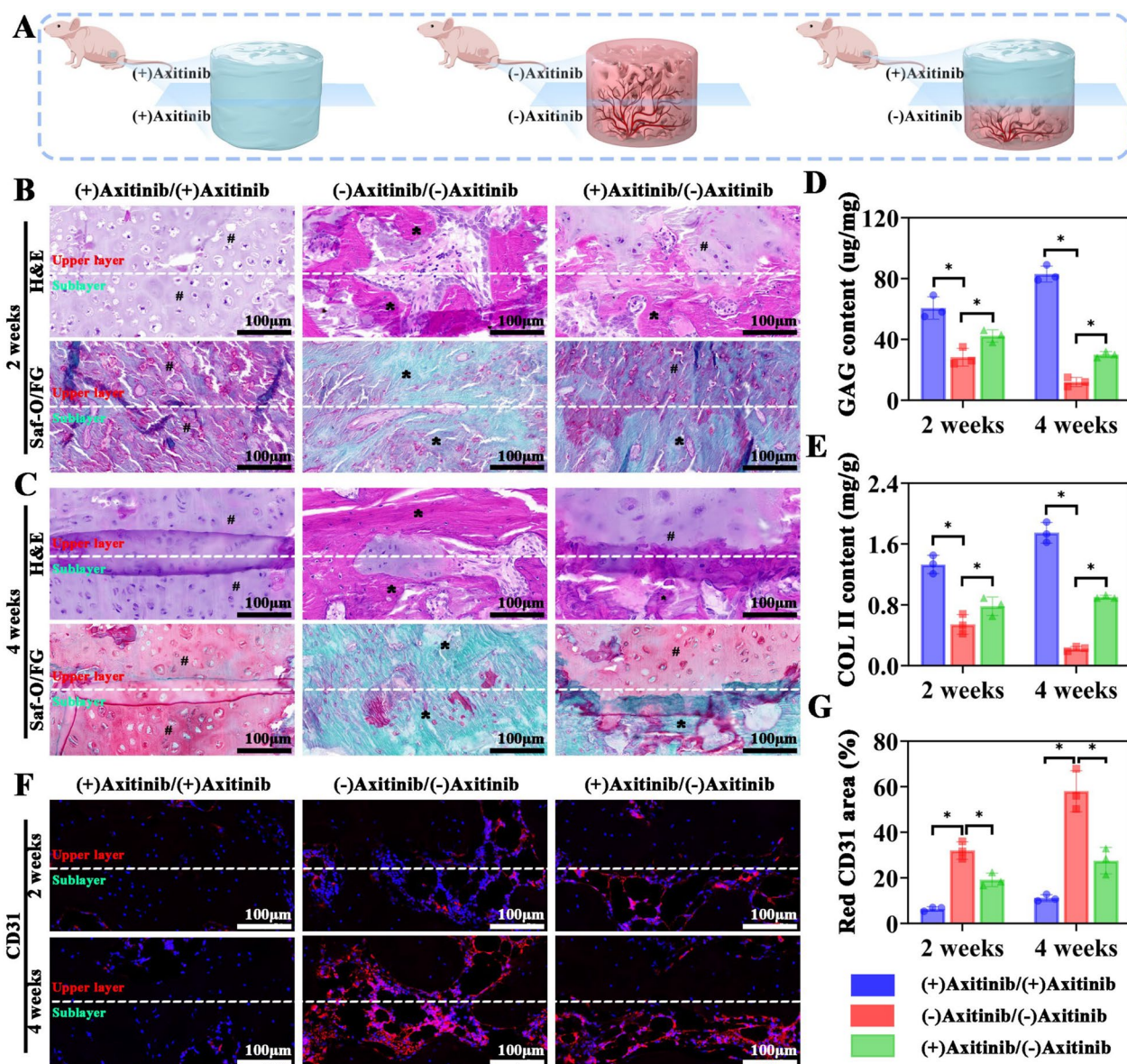


**Fig. 5** In Vivo Chondrogenic and Osteogenic Modulation of Organoid/GelMA Complexes by Avascular and Vascular Microenvironments. **a** Schematic representation of the subcutaneous implantation of organoid/GelMA complexes in nude mice. The complexes were divided into two layers, with the upper and lower layers treated with or without Axitinib, resulting in three groups: (+)Axitinib/(+)Axitinib, (-)Axitinib/(-)Axitinib, and (+)Axitinib/(-)Axitinib. **b, c** Representative H&E and Saf-O/FG staining of implanted organoid/GelMA complexes in the different groups at 2 and 4 weeks. Cartilage matrix is denoted by #, and bone matrix is denoted by \*. The upper and lower layers are delineated by white dashed lines. **d, e** Quantitative analysis of GAG and COL II levels in implanted organoid/GelMA complexes across the groups at 2 and 4 weeks. **f, g** Immunofluorescence staining and quantitative analysis of CD31 expression in implanted organoid/GelMA complexes across the groups at 2 and 4 weeks. n=3; \*p<0.05

groups based on Axitinib loading in the upper and lower layers: (1) (+)Axitinib/(+)Axitinib group (both layers contain Axitinib), (2) (-)Axitinib/(-)Axitinib group (no Axitinib in either layer), and (3) (+)Axitinib/(-)Axitinib group (Axitinib only in the upper layer).

H&E and Saf-O/FG staining at 2 weeks post-implantation revealed homogeneous cartilage tissue regeneration

in the (+)Axitinib/(+)Axitinib group and bone tissue regeneration in the (-)Axitinib/(-)Axitinib group. In the (+)Axitinib/(-)Axitinib group, cartilaginous ECM secretion was observed in the upper layer, while osseous ECM deposition occurred in the lower layer (Fig. 5b). This pattern became more pronounced at 4 weeks (Fig. 5c). Quantitative analysis showed higher GAG and COL II

levels in the Axitinib-loaded groups, with increasing levels from 2 to 4 weeks (Fig. 5d, e). Micro-CT imaging further confirmed greater osseous ECM deposition and bone trabecula formation in the Axitinib-free layers, with an increasing trend observed from 2 to 4 weeks (Fig. S11a, Supplemental Information). Quantification of Tb.N and Tb.Th confirmed higher values in the Axitinib-free layers (Fig. S11b, c, Supplemental Information), supporting the inhibition of osseous feature production by Axitinib.

CD31 immunofluorescence staining and quantification of the subcutaneous regenerated tissue revealed sparse CD31 expression in the Axitinib-loaded layers and abundant CD31 expression in the Axitinib-free layers (Fig. 5f, g). These results underscore the vascular microenvironment as a key determinant in directing the endochondral ossification of cartilage organoids. In conclusion, this study successfully established an avascular microenvironment via Axitinib treatment in a nude mouse model, demonstrating that osseous regeneration occurred in the Axitinib-free layers while cartilage regeneration was observed in the Axitinib-loaded layers.

#### **Gradient heterogeneous osteochondral regeneration of organoid/GelMA cylinder in a rabbit OCD model**

To facilitate integrative osteochondral regeneration, we prepared an intact organoid/GelMA cylinder for in situ osteochondral implantation. An OCD model was established in rabbit knee joints, with three treatment groups: an empty group (control), a pure GelMA cylinder implantation group, and an organoid/GelMA cylinder implantation group (Fig. 6a). At 12 weeks post-surgery, gross observations revealed limited tissue repair in the empty group, while the GelMA and organoid/GelMA groups showed improved tissue repair. Notably, in the organoid/GelMA group, newly formed tissue integrated seamlessly with the surrounding native cartilage, closely resembling the natural state (Fig. 6b). 3D micro-CT imaging confirmed these differences among groups, in line with the gross observations (Fig. 6b). Additionally, 2D micro-CT images showed the highest levels of newly formed bone trabeculae in the organoid/GelMA group, intermediate levels in the GelMA group, and the lowest levels in the empty group (Fig. 6b). Quantitative analysis of repaired joint tissue demonstrated that the organoid/GelMA group achieved the highest ICRS histological scores, as well as the highest osseous-related BV/TV and Tb.Th levels, confirming superior osteochondral regeneration in this group (Fig. 6c).

H&E staining revealed distinct differences among the three groups in the cartilage layer, transitional layer, and subchondral bone layer (Fig. 6d). In the empty group, defects were present across all three layers. In the GelMA

group, defects remained in the cartilage layer, the transitional layer was undetectable, and the subchondral bone layer was present. In contrast, the organoid/GelMA group showed well-integrated cartilage and transitional layers, along with an intact subchondral bone layer.

Saf-O/FG staining provided detailed insights into the cartilage and bone ECM. In the empty group, neither cartilage nor bone ECM was stained, indicating a lack of osteochondral regeneration. In the GelMA group, bone ECM was present in the subchondral bone and transitional layers, but no cartilage ECM was detected in the cartilage layer. In the organoid/GelMA group, the cartilage layer was intensely stained orange-red, indicating mature cartilage deposition, while the subchondral bone was stained blue, indicating mature bone formation. The transitional layer displayed a natural gradient and was perfectly integrated with both the cartilage and subchondral bone layers (Fig. 6e).

Additional evidence was provided by toluidine blue staining and COL II immunohistochemical analysis. Toluidine blue staining showed cartilage tissue in the cartilage layer and the upper half of the transitional layer in the organoid/GelMA group, with no cartilage regeneration observed in the empty or GelMA-only groups (Fig. S12a, Supplemental Information). Similarly, COL II immunostaining was observed exclusively in the cartilage layer and the upper half of the transitional layer in the organoid/GelMA group (Fig. S12b, Supplemental Information).

The biosafety of the organoid/GelMA cylinder was also assessed. H&E staining revealed normal structural morphology in the major organs of rabbits across all groups at 12 weeks post-implantation (Fig. S13a, Supplemental Information). Quantitative analysis of routine blood, liver function, and kidney function tests showed no significant systemic toxicity among the three groups (Fig. S13b, Supplemental Information), demonstrating the safety of the organoid/GelMA cylinder for in vivo use.

In summary, these results provide strong evidence for gradient heterogeneous osteochondral regeneration facilitated by the organoid/GelMA cylinder, driven by the modulation of the natural gradient vascular microenvironment. This supports our hypothesis that a single stem cell-derived organoid can achieve gradient heterogeneous osteochondral regeneration. The successful regeneration of osteochondral tissue using single cartilage organoids can be attributed to the following factors: (1) P3 BMSCs were selected to ensure cell purity while maintaining optimal cell morphology, proliferation capacity, and multidirectional differentiation potential; (2) A favorable 3D culture system in chondrogenic medium was employed to successfully generate cartilage organoids. The 3D environment enhanced cell–cell and cell–ECM

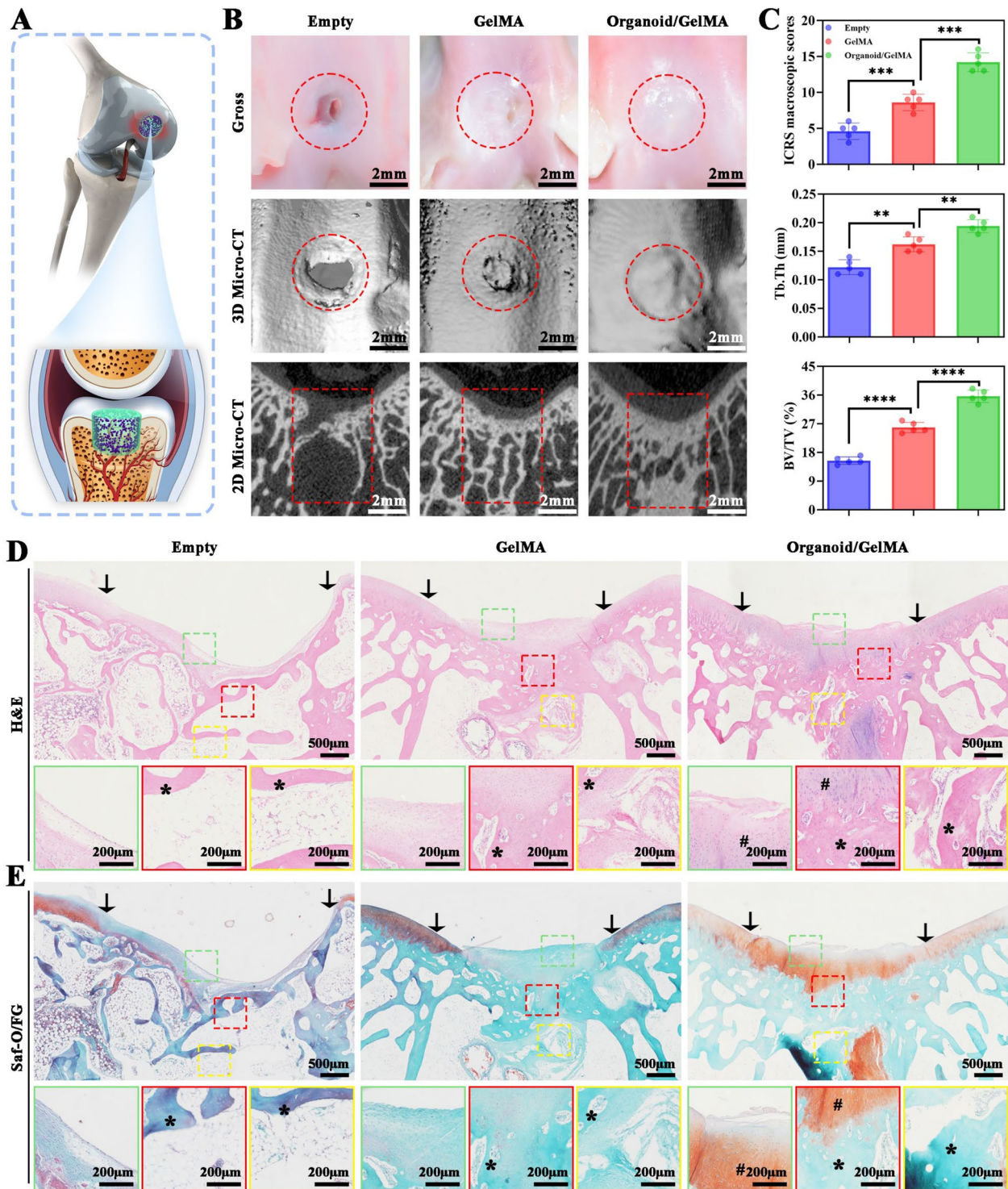


**Fig. 6** Gradient Heterogeneous Osteochondral Regeneration by Organoid/GelMA Cylinder Guided by a Gradient Vascular Microenvironment in a Rabbit OCD Model. **a** Schematic representation of gradient heterogeneous osteochondral regeneration in a rabbit OCD model via in situ implantation of organoid/GelMA cylinder. **b** Gross observation, 3D reconstruction, and 2D imaging of repaired joint tissue at 12 weeks post-treatment in the empty, GelMA, and organoid/GelMA groups. Red dotted circles and squares indicate the OCD regions. **c** Quantitative analysis of ICRS macroscopic scores, Tb.Th, and BV/TV for the regenerated joint tissue in the empty, GelMA, and organoid/GelMA groups.  $n = 5$ ;  $**p < 0.01$ ,  $***p < 0.001$ ,  $****p < 0.0001$ . Representative **d** H&E and **e** Saf-O/FG staining of regenerated joint tissue at 12 weeks. OCD areas are highlighted by two black arrows. Enlarged views of the cartilaginous zone (green squares), transition zone (red squares), and subchondral osseous zone (yellow squares) are shown. Cartilage matrix is denoted by #, and bone matrix is denoted by \*

interactions, promoting superior proliferation, improved cell morphology, and better stemness maintenance; (3) Both in vitro studies and subcutaneous implantation in nude mice showed that the organoid/GelMA complex could regenerate cartilage ECM under avascular conditions, while the vascular niche guided bone ECM regeneration; (4) The organoid/GelMA cylinder implanted at the OCD site integrated to form an intact platform for gradient heterogeneous osteochondral regeneration; (5) In native joint tissue, the cartilage, calcified cartilage transitional, and subchondral bone layers form a gradient vascular microenvironment, transitioning from an avascular niche in the upper layer to a vascular niche in the lower layer. This natural gradient vascular microenvironment played a pivotal role in enabling osteochondral regeneration in the rabbit OCD model following the implantation of the organoid/GelMA cylinder.

## Conclusion

This study demonstrates the feasibility and efficacy of using single BMSC-derived cartilage organoids for gradient heterogeneous osteochondral regeneration. By leveraging the natural vascularization gradient within osteochondral tissue, we successfully guided the site-specific differentiation of cartilage organoids into chondrocytes and osteoblasts, achieving simultaneous cartilage and bone regeneration. The introduction of pro-vascular and anti-vascular microenvironments further highlighted the critical role of vascularization in modulating the osteogenic and chondrogenic differentiation processes. The implantation of organoid/GelMA complexes into rabbit osteochondral defects confirmed the translational potential of this strategy, offering a robust and clinically relevant approach to address the challenges of heterogeneous osteochondral repair. This work provides a promising foundation for future advancements in regenerative medicine and tissue engineering.

## Supplementary Information

The online version contains supplementary material available at <https://doi.org/10.1186/s12951-025-03403-0>.

Additional file 1.

## Author contributions

Zhenying Chen: Conceptualization, Methodology, Software, Formal analysis, Writing—original draft, Formal analysis. Qitao Bo: review and editing, Validation, Investigation. Chao Wang: Validation, Investigation, Methodology. Yong Xu and Xiang Fei: Investigation, Validation, Supervision, Funding acquisition. Ru Chen: review and editing, Supervision, Funding acquisition.

## Funding

This research was supported by National Natural Science Foundation of China (82302395 and 82360560), Hainan Province Clinical Medical Center, Hainan Provincial Natural Science Foundation (ZDYF2020130), Young Elite Scientists

Sponsorship Program by CAST (2023QNRC001), Shanghai Sailing Program (22YF1437400), and Shanghai Rising-Star Program (24QB2704800).

## Data availability

No datasets were generated or analysed during the current study.

## Declarations

### Ethics approval and consent to participate

This study was conducted in accordance with the ethical principles of the Declaration of Helsinki. All animal experiments were approved by the Institutional Animal Care and Use Committee (IACUC) of Shanghai Pulmonary Hospital (Approval No. K23-170Y). Informed consent was obtained from all animal owners prior to participation. All animal procedures were performed following institutional guidelines and in compliance with national regulations regarding animal care and use. The authors confirm that all ethical standards were strictly adhered to throughout the course of the research.

### Competing interests

The authors declare no competing interests.

### Author details

<sup>1</sup>Department of Breast Surgery, Hainan General Hospital (Hainan Affiliated Hospital of Hainan Medical University), Haikou, China. <sup>2</sup>The Center of Joint and Sports Medicine, Orthopedics Department, Zhongda Hospital, School of Medicine, Southeast University, Nanjing, China. <sup>3</sup>Department of Thoracic Surgery, Shanghai Pulmonary Hospital, School of Medicine, Tongji University, Shanghai, China. <sup>4</sup>Department of Plastic and Burn Surgery, the Second Affiliated Hospital of Chengdu Medical College, China National Nuclear Corporation 416 Hospital, Chengdu, China.

Received: 6 February 2025 Accepted: 15 April 2025

Published online: 29 April 2025

## References

- Lin X, Zhang Y, Li J, Oliver BG, Wang B, Li H, Yong K-T, Li JJ. Biomimetic multizonal scaffolds for the reconstruction of zonal articular cartilage in chondral and osteochondral defects. *Bioact Mater.* 2025;43:510–49.
- Xiong Z, Hong F, Wu Z, Ren Y, Sun N, Heng BC, Zhou J. Gradient scaffolds for osteochondral tissue engineering and regeneration. *Chem Eng J.* 2024;498: 154797.
- Gao W, Chen K, He W, Zhao S, Cui D, Tao C, Xu Y, Xiao X, Feng Q, Xia H. Synergistic chondrogenesis promotion and arthroscopic articular cartilage restoration via injectable dual-drug-loaded sulfated hyaluronic acid hydrogel for stem cell therapy. *Compos B Eng.* 2023;263: 110857.
- Cao R, Xu Y, Xu Y, Brand DD, Zhou G, Xiao K, Xia H, Czernuszka JT. Development of tri-layered biomimetic Atelocollagen scaffolds with interfaces for osteochondral tissue engineering. *Adv Healthcare Mater.* 2022;11(11): e2101643.
- Hinckel BB, Thomas D, Vellios EE, Hancock KJ, Calcei JG, Sherman SL, Eliasberg CD, Fernandes TL, Farr J, Lattermann C, Gomoll AH. Algorithm for treatment of focal cartilage defects of the knee: classic and new procedures. *Cartilage.* 2021;13(1\_suppl):473S-495S.
- Dai W, Cheng J, Yan W, Cao C, Zhao F, Li Q, Hu X, Wang J, Ao Y. Enhanced osteochondral repair with hyaline cartilage formation using an extracellular matrix-inspired natural scaffold. *Sci Bull.* 2023;68(17):1904–17.
- Huang B, Li P, Chen M, Peng L, Luo X, Tian G, Wang H, Wu L, Tian Q, Li H, Yang Y, Jiang S, Yang Z, Zha K, Sui X, Liu S, Guo Q. Hydrogel composite scaffolds achieve recruitment and chondrogenesis in cartilage tissue engineering applications. *J Nanobiotechnol.* 2022;20(1):25.
- Griffin M, Kalaskar D, Butler P. Argon plasma modified nanocomposite polyurethane scaffolds provide an alternative strategy for cartilage tissue engineering. *J Nanobiotechnol.* 2019;17(1):51.
- Di Martino A, Salerno M, Galassi E, Grillini L, Dotti A, De Luca C, Filardo G. Osteochondral regeneration with a tri-layered biomimetic resorbable scaffold: in vivo study in a sheep model up to 12 months of follow-up. *Biomaterials.* 2025;314: 122821.

10. Kim W, Gwon Y, Park S, Kim H, Kim J. Therapeutic strategies of three-dimensional stem cell spheroids and organoids for tissue repair and regeneration. *Bioact Mater.* 2023;19:50–74.
11. Smith E, Cochran WJ. Cystic organoid teratoma: (report of a case). *Can Med Assoc J.* 1946;55(2):151–2.
12. Sato T, Vries RG, Snippert HJ, van de Wetering M, Barker N, Stange DE, van Es JH, Abo A, Kujala P, Peters PJ, Clevers H. Single Lgr5 stem cells build crypt-villus structures in vitro without a mesenchymal niche. *Nature.* 2009;459(7244):262–5.
13. Zhao Z, Chen X, Dowbaj AM, Sljukic A, Bratlie K, Lin L, Fong ELS, Balachander GM, Chen Z, Soragni A, Huch M, Zeng YA, Wang Q, Yu H. Organoids. *Nature Rev Methods Primers.* 2022;2(1):94.
14. Schröter-Kermani C, Hinz N, Risse P, Zimmermann B, Merker HJ. The extracellular matrix in cartilage organoid culture: biochemical, immunomorphological and electron microscopic studies. *Matrix (Stuttgart, Germany).* 1991;11(6):428–41.
15. Irie Y, Mizumoto H, Fujino S, Kajiwara T. Development of articular cartilage grafts using organoid formation techniques. *Transpl Proc.* 2008;40(2):631–3.
16. Wang Y, You Y, Chen H, Liu J, Wu Q, Dai K, Sun Y. 3D-bioprinted anti-senescence organoid scaffolds repair cartilage defect and prevent joint degeneration via miR-23b/ELOVL5-mediated metabolic rewiring. *Chem Eng J.* 2024;491: 152049.
17. Iordachescu A, Hughes EAB, Joseph S, Hill EJ, Grover LM, Metcalfe AD. Trabecular bone organoids: a micron-scale 'humanised' prototype designed to study the effects of microgravity and degeneration. *NPJ Microgravity.* 2021;7(1):17.
18. Dai K, Zhang Q, Deng S, Yu Y, Zhu F, Zhang S, Pan Y, Long D, Wang J, Liu C. A BMP-2-triggered in vivo osteo-organoid for cell therapy. *Sci Adv.* 2023;9(1):eadd1541.
19. Gao E, Wang Z, Zhao S, Zhu X, Xu S, Xu Y, Wang Y, Xu N, Tao B. Core-shell structured nanomembrane with sequential immune and vascular isolation effects followed by chondrogenic induction to promote stable stem cell-based subcutaneous cartilage regeneration in large animals. *Chem Eng J.* 2024;498: 154878.
20. He W, Li C, Zhao S, Li Z, Wu J, Li J, Zhou H, Yang Y, Xu Y, Xia H. Integrating coaxial electrospinning and 3D printing technologies for the development of biphasic porous scaffolds enabling spatiotemporal control in tumor ablation and osteochondral regeneration. *Bioact Mater.* 2024;34:338–53.
21. Arai Y, Cha R, Nakagawa S, Inoue A, Nakamura K, Takahashi K. Cartilage Homeostasis under Physioxia. *Int J Mol Sci.* 2024;25(17):9398.
22. Zhang H, Wang L, Cui J, Wang S, Han Y, Shao H, Wang C, Hu Y, Li X, Zhou Q, Guo J, Zhuang X, Sheng S, Zhang T, Zhou D, Chen J, Wang F, Gao Q, Jing Y, Chen X, Su J. Maintaining hypoxia environment of subchondral bone alleviates osteoarthritis progression. *Sci Adv.* 2023;9(14):eabo7868.
23. Wu D, Zheng K, Yin W, Hu B, Yu M, Yu Q, Wei X, Deng J, Zhang C. Enhanced osteochondral regeneration with a 3D-Printed biomimetic scaffold featuring a calcified interfacial layer. *Bioact Mater.* 2024;36:317–29.
24. Yang Y, Wu Y, Yang D, Neo SH, Kadir ND, Goh D, Tan JX, Denslin V, Lee EH, Yang Z. Secretive derived from hypoxia preconditioned mesenchymal stem cells promote cartilage regeneration and mitigate joint inflammation via extracellular vesicles. *Bioact Mater.* 2023;27:98–112.
25. Chen L, Huang X, Chen H, Bao D, Su X, Wei L, Hu N, Huang W, Xiang Z. Hypoxia-mimicking scaffolds with controlled release of DMOG and PTHrP to promote cartilage regeneration via the HIF-1 $\alpha$ /YAP signaling pathway. *Int J Biol Macromol.* 2023;226:716–29.
26. Theodoridis K, Aggelidou E, Manthou ME, Kritis A. Hypoxia promotes cartilage regeneration in cell-seeded 3D-printed bioscaffolds cultured with a bespoke 3D culture device. *Int J Mol Sci.* 2023;24(7):6040.
27. Wei J, Duan D, Jing Y, Huang S, Liu J, Lou A, Xiao T, Chen Y, Chen X, Zeng Y, Liu S, Wang Z, Yang Y, Zhou L, Wu Z, Wang L. Heparin-conjugated injectable hydrogels with sustained releasing capability for promotion of H-type vessels formation and rat femoral bone defects repair. *Mater Des.* 2023;235: 112407.
28. Saberi A, Kouhjani M, Mohammadi M, Hosta-Rigau L. Novel scaffold platforms for simultaneous induction osteogenesis and angiogenesis in bone tissue engineering: a cutting-edge approach. *J Nanobiotechnol.* 2023;21(1):351.
29. Yan C, Zhang P, Qin Q, Jiang K, Luo Y, Xiang C, He J, Chen L, Jiang D, Cui W, Li Y. 3D-printed bone regeneration scaffolds modulate bone metabolic homeostasis through vascularization for osteoporotic bone defects. *Biomaterials.* 2024;311: 122699.
30. Zou J, Du C, Liu S, Zhao P, Gao S, Chen B, Wu X, Huang W, Zhu Z, Liao J. Notch1 signaling regulates Sox9 and VEGFA expression and governs BMP2-induced endochondral ossification of mesenchymal stem cells. *Genes Dis.* 2024;12: 101336.
31. Yu Y, Li P, Zhu C, Ning N, Zhang S, Vancso GJ. Multifunctional and recyclable photothermally responsive cryogels as efficient platforms for wound healing. *Adv Funct Mater.* 2019;29(35):1904402.
32. Xu Y, Dai J, Zhu X, Cao R, Song N, Liu M, Liu X, Zhu J, Pan F, Qin L, Jiang G, Wang H, Yang Y. Biomimetic trachea engineering via a modular ring strategy based on bone-marrow stem cells and atelocollagen for use in extensive tracheal reconstruction. *Adv Mater.* 2022;34(6):2106755.
33. Lei Q, He D, Ding L, Kong F, He P, Huang J, Guo J, Brinker CJ, Luo G, Zhu W, Yu Y. Microneedle patches integrated with biomaterialized melanin nanoparticles for simultaneous skin tumor photothermal therapy and wound healing. *Adv Funct Mater.* 2022;32(22):2113269.
34. Xu N, Yuan Y, Ding L, Li J, Jia J, Li Z, He D, Yu Y. Multifunctional chitosan/gelatin@tannic acid cryogels decorated with in situ reduced silver nanoparticles for wound healing. *Burns Trauma.* 2022;10:tkac019.
35. Xu N, Gao Y, Li Z, Chen Y, Liu M, Jia J, Zeng R, Luo G, Li J, Yu Y. Immunoregulatory hydrogel decorated with Tannic acid/Ferric ion accelerates diabetic wound healing via regulating Macrophage polarization. *Chem Eng J.* 2023;466: 143173.
36. Morin GB. The human telomere terminal transferase enzyme is a ribonucleoprotein that synthesizes TTAGGG repeats. *Cell.* 1989;59(3):521–9.
37. Kremer LPM, Cerrizuela S, El-Sammak H, Al Shukairi ME, Ellinger T, Straub J, Korkmaz A, Volk K, Brunken J, Kleber S, Anders S, Martin-Villalba A. DNA methylation controls stemness of astrocytes in health and ischaemia. *Nature.* 2024;634(8033):415–23.
38. Wang K, Zhang T, Dong Q, Nice EC, Huang C, Wei Y. Redox homeostasis: the linchpin in stem cell self-renewal and differentiation. *Cell Death Dis.* 2013;4(3):e537–e537.
39. Tao B, Xu T, Yu L, Zhang L, Cao G, Gong N, Zhou G, Xiao K, Huo Y, Xia H. A simple and low-cost method to develop porous egg white scaffolds with controllable shape for cartilage regeneration. *Compos B Eng.* 2025;295: 112192.
40. Sulaiman S, Chowdhury SR, Fauzi MB, Rani RA, Yahaya NHM, Tabata Y, Hiraoka Y, Binti Haji Idrus R, Min Hwei N. 3D culture of MSCs on a gelatin microsphere in a dynamic culture system enhances chondrogenesis. *Int J Mol Sci.* 2020;21(8):2688.
41. Shanbhag S, Suliman S, Mohamed-Ahmed S, Kamleitner C, Hassan MN, Heimel P, Dobsak T, Tangl S, Bolstad AI, Mustafa K. Bone regeneration in rat calvarial defects using dissociated or spheroid mesenchymal stromal cells in scaffold-hydrogel constructs. *Stem Cell Res Ther.* 2021;12(1):575.
42. Yu L, Wu Y, Liu J, Li B, Ma B, Li Y, Huang Z, He Y, Wang H, Wu Z, Qiu G. 3D culture of bone marrow-derived mesenchymal stem cells (BMSCs) could improve bone regeneration in 3D-printed porous Ti6Al4V scaffolds. *Stem Cells Int.* 2018;2018:2074021.
43. Le HA, Mayor R. Cell–matrix and cell–cell interaction mechanics in guiding migration. *Biochem Soc Trans.* 2023;51(4):1733–45.
44. Guo L, Liu X, Wang Y, Yi J, Li J, Xu Y, Cai K, Dai W, Feng Q, Tao B. Enhancing long-segmental tracheal restoration: a self-repairing hydrogel loaded with chondrocytokines for sutureless anastomosis and cartilage regeneration. *Mater Today Bio.* 2024;28: 101208.

## Publisher's Note

Springer Nature remains neutral with regard to jurisdictional claims in published maps and institutional affiliations.